Additively Manufactured Millimeter-Wave Dual-Band Single-Polarization Shared Aperture Fresnel Zone Plate Metalens Antenna

Jianfeng Zhu, *Member, IEEE*, Yang Yang, *Senior Member, IEEE*, Mengze Li, *Student Member, IEEE*, David McGloin, Shaowei Liao, *Senior Member, IEEE*, Jaim Nulman, *Senior Member, IEEE*, Minoru Yamada, and Francesca Iacopi, *Senior Member, IEEE*

***Abstract*— Fresnel zone plate (FZP) lens antenna, consisting of a set of alternative transparent and opaque concentric rings arranged on curvilinear or flat surfaces, have been widely used in various fields for sensing and communications. Nevertheless, the state-of-art FZP lens antennas are limited to a single band due to the frequency-dependent feature, which hinders their use in multi-band applications. In this work, a shared aperture dual-band FZP metalens antenna is proposed by merging two single-band FZP metalens antenna operating at distinct frequency bands seamlessly into one. Instead of using conventional metallic conductors, double-screen metagrids are devised in this work to form the concentric rings. Because the metagrids show distinct transmission/reflection properties at different frequencies, the performance of one set of concentric rings operating at the one band will not be affected by the other operating at the different band. In addition, to compensate for the phase shift introduced by the metagrids, an additional dielectric ring layer is added atop the FZP taking advantage of additive manufacturing. Thus, the radiation performance of the dual-band FZP lens antenna is comparable to that of each single FZP metalens antenna. For proof-of-concept, an antenna prototype operating at the dual band, 75 and 120 GHz with a frequency ratio of 1.6, is fabricated using an integrated additively manufactured electronics (AME) technique. The measured peak gains of 20.3 and 21.9 dBi are achieved at 75 and 120 GHz, respectively.**

***Index Terms*— Additive manufacturing, dual-band, Fresnel zone plate (FZP), metalens antenna, millimeter-wave (mm-wave).**

Manuscript received October 27, 2020; revised February 18, 2021; accepted March 2, 2021. Date of publication April 6, 2021; date of current version October 6, 2021. This work was supported by the Nano Dimension through a Ph.D. Scholarship Agreement and UTS FEIT Blue Sky Grant. *(Corresponding author: Yang Yang.)*

Jianfeng Zhu, Yang Yang, Mengze Li, and David McGloin are with the School of Electrical and Data Engineering, University of Technology Sydney, Ultimo, NSW 2007, Australia (e-mail: yang.yang.au@ieee.org).

Shaowei Liao is with the Guangdong Principle Key Laboratory of Millimeter-Wave and Terahertz, School of Electronic and Information Engineering, South China University of Technology, Guangzhou 510641, China.

Jaim Nulman and Minoru Yamada are with Nano Dimension, Sunrise, FL 33325 USA.

Francesca Iacopi is with the School of Electrical and Data Engineering, University of Technology Sydney, Ultimo, NSW 2007, Australia, and also with the Australian Research Council Centre of Excellence in Transformative Meta-Optical Systems, School of Electrical and Data Engineering, University of Technology Sydney, NSW 2007, Australia.

Color versions of one or more figures in this article are available at https://doi.org/10.1109/TAP.2021.3070224.

Digital Object Identifier 10.1109/TAP.2021.3070224

I. Introduction

MILLIMETER-WAVE (mm-wave) and terahertz (THz) technologies create a new era of many emerging research areas, such as high-resolution imaging, high-speed big data communications, and ubiquitous sensing [1]–[6]. Since the mm-wave spectrum is located between the microwave and optical regions, its development provides an opportunity to consolidate and reconcile the paradigms of microwave engineering with optics and photonics [7]–[9]. Nevertheless, the general hurdles of mm-wave technology are the tremendous loss and the quasi-optical propagation path of communication link [10]. In addition, mm-wave signals also experience extra atmospheric attenuation when compared with lower electromagnetic (EM) frequencies. As a result, mm-wave communications are mainly restricted to line-of-sight (LOS). To tackle these challenges, large-scale antenna arrays are tightly packed in the transceiver front-end to compensate for the high path loss and bridge the gap of link budget, albeit rather bulky. As an alternative approach, lenses or transmitarrays that can collimate the EM waves from the source are used to obtain highly directional beams. Over the past decade, various kinds of mm-wave lenses and transmitarrays based on the concept of metasurface have been proposed to meet the requirement of different mm-wave application scenarios [11]–[24]. Nevertheless, to achieve flexible phase control over a broad span covering the range $[-\pi, \pi]$ of the wavefront, the "meta-atoms" are usually implemented by cascading several resonant cells in a multilayered form with bonding process. Moreover, many state-of-art mm-wave metalenses and transmitarrays are limited to a single band [15]–[22]. To achieve dual-band feature, most of the metalenses or transmitarrays use orthogonal polarization for phase control over two bands [23]–[26]. Dual-band single-polarization mm-wave metalenses and transmitarrays are rarely reported because it is difficult for the "meta-atoms" to achieve dual-band/multi-band phase control of the wavefront independently in a single polarization. As for prototyping, state-of-the-art mm-wave lenses and transmitarrays use printed circuit board (PCB) to fabricate each layer independently and stacked them together. 3-D printing, also known as additive manufacturing, has

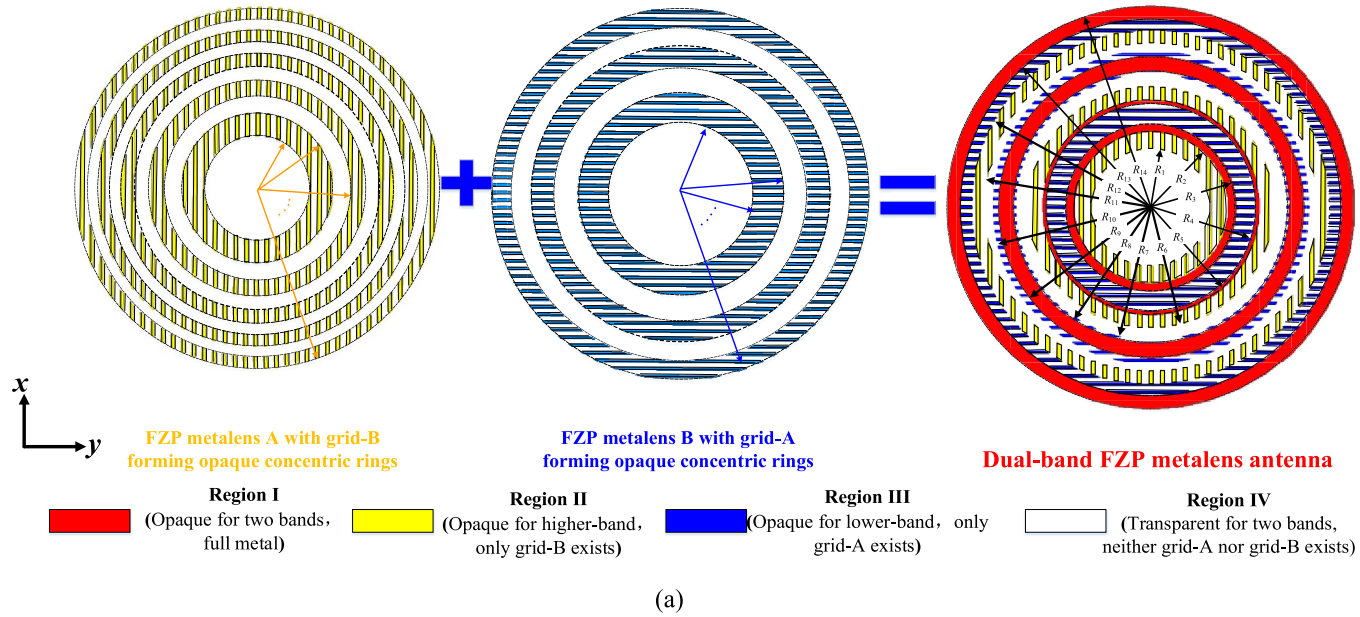

(a)

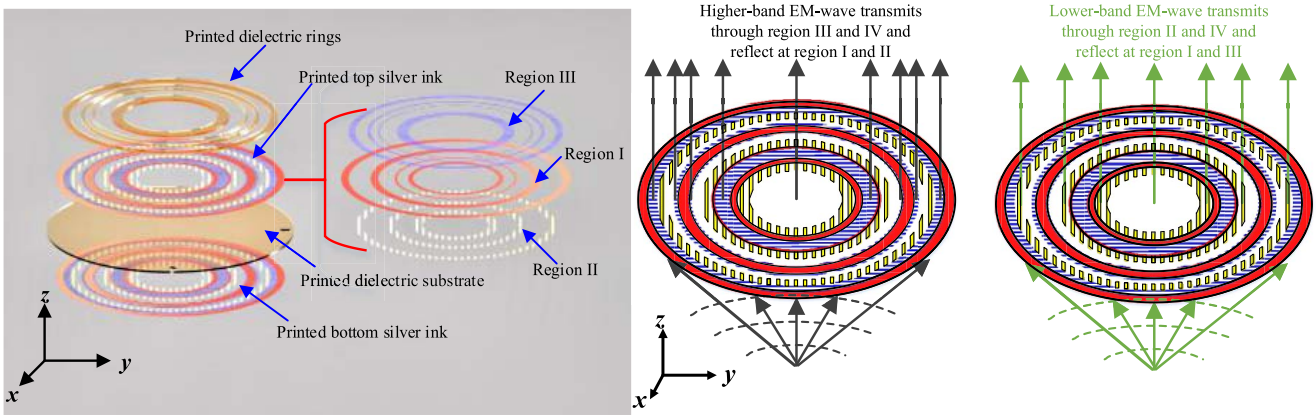

(b) (c) (d)

Fig. 1. (a) Design concept of the proposed dual-band FZP metalens antenna, which is implemented by merging two single-band FZP metalens antennas (FZP metalens A: operating at the high band and FZP metalens B: operating at the low band. $R_1 = 8.75$ mm, $R_2 = 11.13$ mm, $R_3 = 12.5$ mm, $R_4 = 15.4$ mm, $R_5 = 16$ mm, $R_6 = 18$ mm, $R_7 = 19.9$ mm, $R_8 = 20.34$ mm, $R_9 = 22.5$ mm, $R_{10} = 23.32$ mm, $R_{11} = 24.5$ mm, $R_{12} = 26.45$ mm, $R_{13} = 28.21$ mm, and $R_{14} = 29.5$ mm). (b) Configurations of the proposed dual-band FZP lens antenna (not scaled in z-direction). (c) High-band y-polarized EM wave transmits through region III and region IV and reflects at region I and region II. (d) Low-band y-polarized EM wave transmits through region II and region IV and reflects at region I and region III.

offered a new and economical way to build the lenses and transmitarrays. Various kinds of lenses have been proposed using additive manufacturing [27]–[40]. Nevertheless, most of them are dielectric-based. In fact, state-of-the-art works using additive manufacturing are either dielectric printing (coated with metal if required) or directly metal printing. Lenses or transmitarrays using conductive and dielectric integrated additively manufactured electronics (AME) technique have not been reported. However, the one-stop integrated printing can provide more design freedom, that is, both metallic and dielectric structure can be printed simultaneously without post-processing procedure such as bonding, alignment, and coating.

Fresnel zone plate (FZP) lens antenna, implemented by a set of alternative transparent and opaque concentric rings either transmitting or blocking the incident EM wave, has the advantages of a thinner profile and lighter weight than a traditional lens antenna with a drawback of 50% back reflection of energy [41]–[47]. Generally, each zone of the FZP lens antenna is divided into an even number of subzones. The radii (Ri) of each transparent and opaque zone can be determined using [47]

$$R_i = \sqrt{i\lambda_0 F + \left(\frac{i\lambda_0}{2}\right)^2}, \quad i = 1, 2, \ldots, N \tag{1}$$

where λ_0 is the design wavelength, and F is the focal length. Because of spatial dispersion, the diffraction of the FZP lens antenna is frequency-dependent. Thus, a conventional FZP lens antenna can only support a single operating bandwidth. A reconfigurable FZP lens antenna at the microwave region was proposed by using pin diodes to control different states of metasurface to realize dual-band operation [45], but still

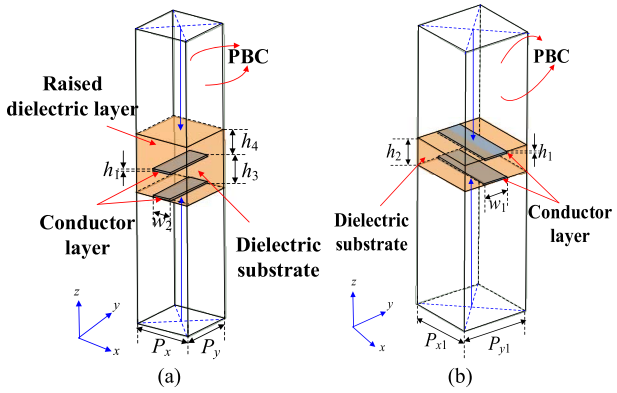

Fig. 2. (a) Grid-A with raised dielectric layer forming region III. (b) Grid-B forming region II ($h_1 = 35\ \mu$m, $h_2 = 0.5$ mm, $h_3 = 0.5$ mm, $h_4 = 0.65$ mm, $w_1 = 0.6$ mm, $w_2 = 0.42$ mm, $P_x = 1.2$ mm, $P_y = 1.2$ mm, $P_{x1} = 1.7$ mm, and $P_{y1} = 1.7$ mm).

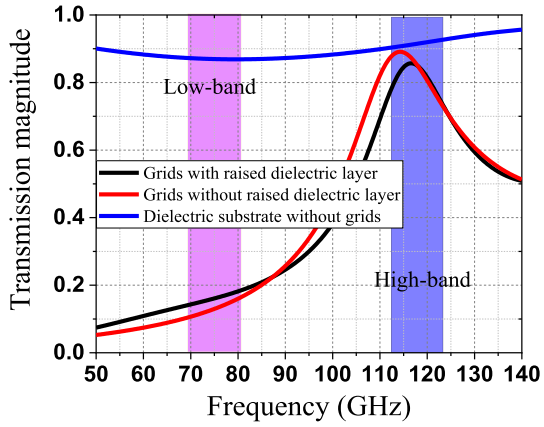

Fig. 3. (a) Simulated transmission magnitude of grid-A with/without raised dielectric layer and dielectric substrate only. (b) Simulated transmission phase of grid-A with/without raised dielectric layer and dielectric substrate only.

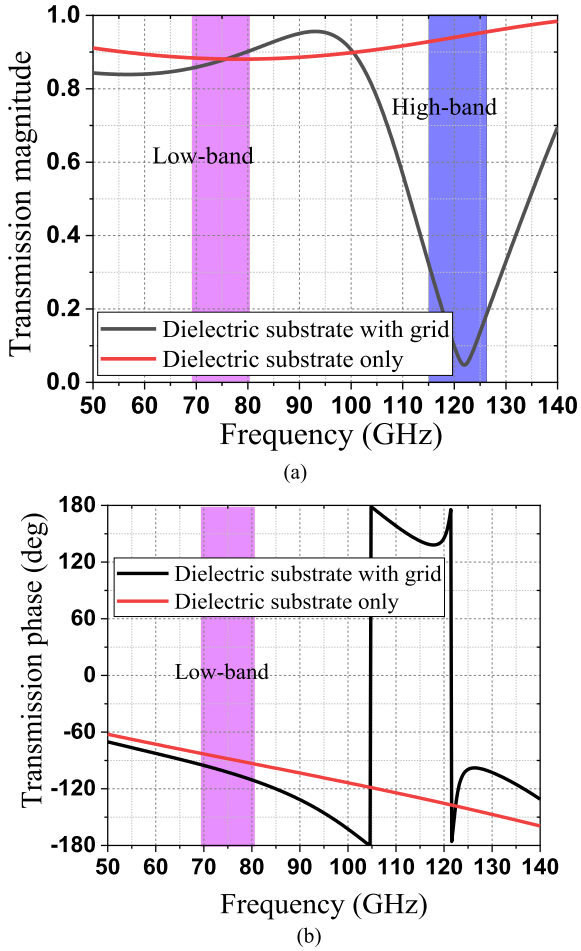

Fig. 4. (a) Simulated transmission magnitude of dielectric with/without grid-B. (b) Simulated transmission phase of dielectric with/without grid-B.

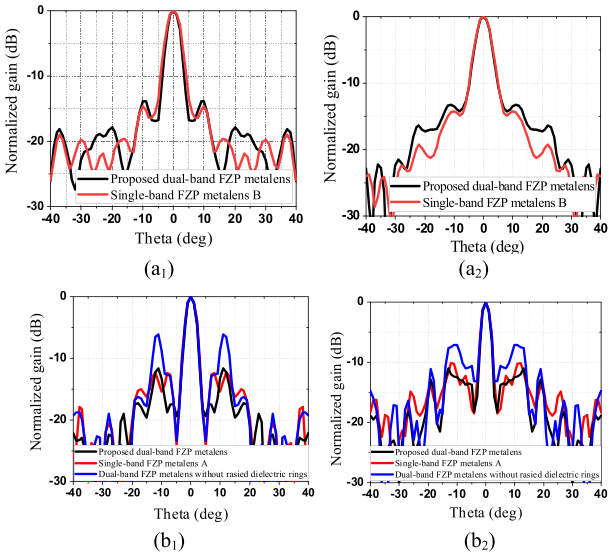

Fig. 5. (a) Radiation performance comparison between the proposed dual-band FZP metalens antenna and the single-band FZP metalens B at 75 GHz. (b) Radiation performance comparison between the proposed dual-band FZP metalens antenna and the single-band FZP metalens A at 120 GHz.

only one diffractive pattern can generate on the aperture at a given state. In addition, the cut-off frequency of the lossy pin diodes hinders the concept from being applied to the mm-wave regions.

In this article, a shared aperture dual-band single-polarization FZP metalens antenna is proposed. Two sets of concentric opaque rings of FZP metalens antennas operating at low-band and high-band are formed using double-screen meta-grids, which show distinct transmission/reflection properties at

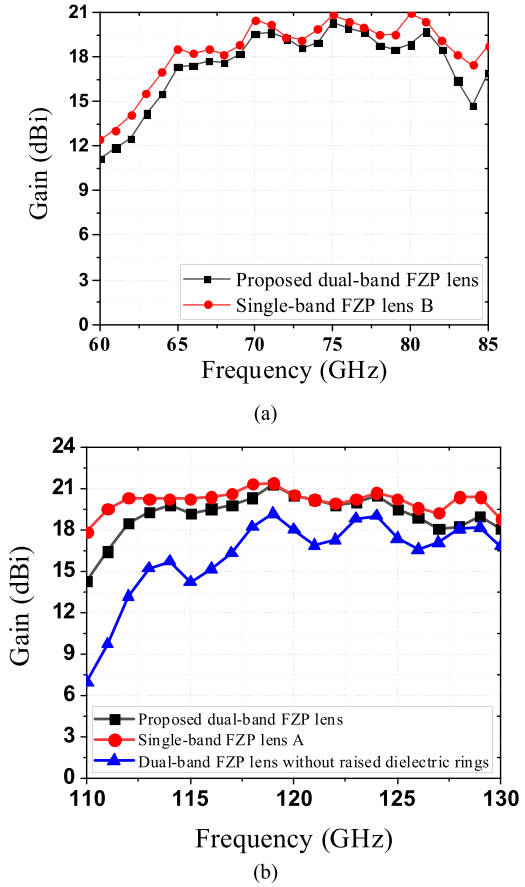

Fig. 6. Boresight gain comparison at two bands. (a) Low band. (b) High band.

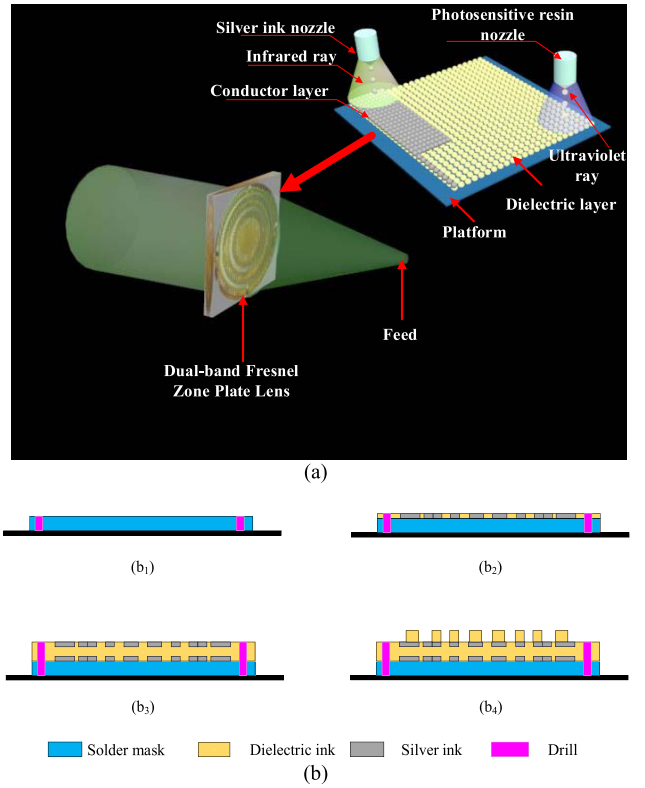

Fig. 7. (a) Proposed dual-band FZP metalens antenna fabricated using integrated conductive/dielectric additive manufacturing. (b) Fabrication steps of the conductive/dielectric one-stop additive manufacturing.

two bands. Then, they are merged in the same aperture seamlessly without affecting each other. Taking advantage of additive manufacturing, an additional dielectric ring layer is added atop the FZP to compensate for the phase shift introduced by the metagrids. Thus, the radiation performance of the dual-band FZP lens antenna is comparable to that of each single FZP metalens antenna. For proof-of-concept, a dual-band FZP metalens antenna operating at 75 and 120 GHz is fabricated using an integrated AME technique. The performance of the FZP metalens antenna has been experimentally verified. It is noted that the design is only chosen as a demonstrative example, and it has the potential to be configured to other frequencies with different frequency ratios.

II. Dual-Band FZP Lens Antenna Design

A. Antenna Geometry

The basic geometry and concept are illustrated in Fig. 1(a) and (b). The proposed dual-band single-polarization FZP metalens antenna is realized by merging two single-band FZP metalens antennas operating at distinct frequency bands into a shared aperture. Since the radii of the concentric rings of two FZP metalens antennas are different, simply placing the rings together will destroy the performance of FZP metalens antenna at both bands. Therefore, instead of using conventional metallic conductors, the concentric rings of two FZP metalens antennas are realized using different double-screen metagrids (grid-A and grid-B), as shown in Fig. 1(a). In this way, the opaque concentric rings of the high-band FZP metalens (formed by grid-B) can reflect the EM waves at the high band while allowing the EM waves at the low band to pass. Similarly, the opaque concentric rings of the low-band FZP metalens (formed by grid-A) can reflect the EM waves at the low band while allowing the EM waves at the high band to pass. Once these opaque concentric rings are combined to form the dual-band FZP metalens, there are four different regions on the aperture of the dual-band FZP metalens, namely, Region I: the overlapped area of grid-A and grid-B, presented by fully conductive layers, reflects the EM wave at both bands. Region II: An opaque area (grid-B) reflects high-band waves, while keeping low-band waves transmitted. Region III: An opaque area (grid-A) reflects low-band waves, while keeping high-band waves transmitted. Region IV: The transparent area (neither grid-A nor grid-B exists) for waves at both bands transmitting through the metalens, as depicted in Fig. 1(a). Thus, for the high band, the transparent part (allowing EM wave to pass) is formed by region III and region IV. Similarly, the transparent part is formed by region II and region IV for low band, as depicted in Fig. 1(c) and (d).

B. Metagrids Design

The crucial factor determining the performance of the proposed dual-band FZP metalens antenna is the double-screen metagrids (grid-A and grid-B) forming concentric

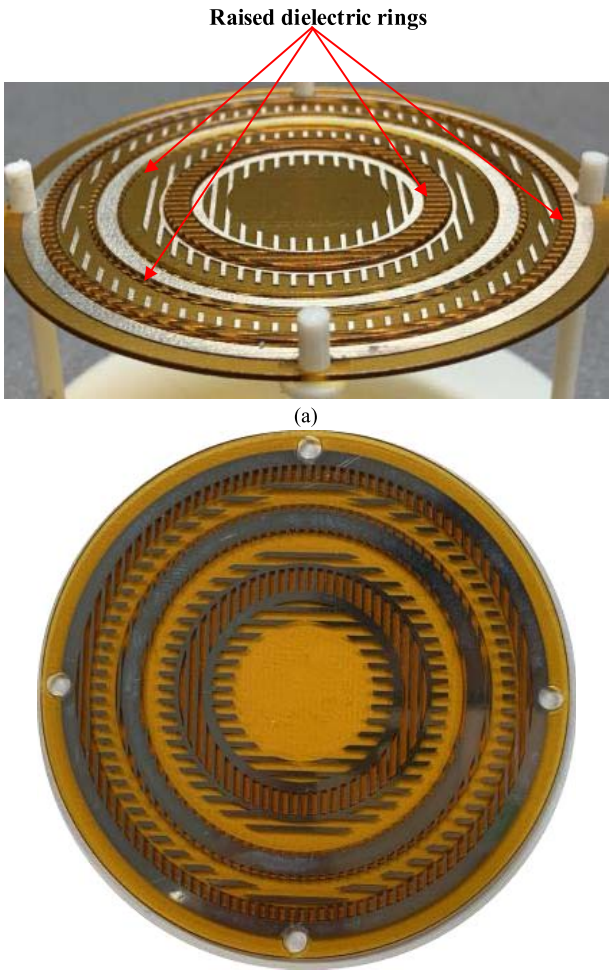

Fig. 8. Photographs of the 3-D printed metalens antenna. (a) 3-D view. (b) Top view.

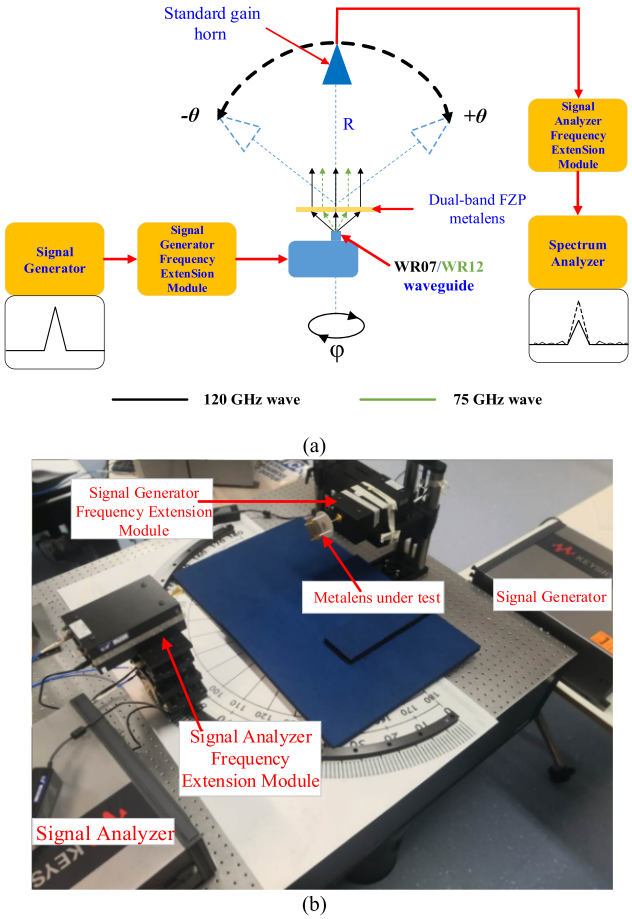

Fig. 9. (a) Block diagram of the measurement system. (b) Proposed FZP metalens antenna under test.

rings operating at low band and high band, as shown in Fig. 2(a) and (b), respectively. EM simulations are carried out in ANSYS HFSS with periodical boundary conditions (PBC). As we know, the function of the metagrids is determined by the period between the parallel grid element. If the metagrid period is long compared with the wavelength, the metagrid functions as a diffraction grating and diffracts both x- and y-polarizations [48]. However, when the metagrid spacing is much smaller than the wavelength, the metagrid functions as a polarizer reflecting incident waves with polarization parallel to the metagrid and transmits the EM wave of the orthogonal polarization. Here, the period of the metagrid is smaller than the wavelength at low band (75 GHz) and the grid-A functions as the polarizer to reflect the EM waves along the y-direction at low band with transmission magnitude as low as around 0.1, as shown in Fig. 3(a). While at high band (120 GHz), the double-screen metagrid functions as an anti-reflection coating with improved transmission magnitude reaching 0.88, demonstrating it allows the high-band EM wave to pass. Nevertheless, the double-screen metagrids also introduce phase abruption into the high-band transmission phase, making it 76° difference compared with the transmission phase of the one without grid-A (region IV) at 120 GHz, as seen from Fig. 3(b). Since region IV and region III (forming by grid-A) are both transparent for the EM waves at high band, additional phase compensating is required, enabling two regions to have the same transmission phase. Taking advantage of additive manufacturing, a dielectric layer with a thickness of 0.65 mm is added atop of grid-A for phase compensating. After adding the phase-compensating dielectric layer, the transmission magnitude only slightly shifts to a higher frequency while the transmission phase of region III and region IV becomes nearly the same at 120 GHz, as shown in Fig. 3(b).

As for region II, although the configuration of grid-B forming region II is similar to grid-A, the reflection principle is different. The reflection of y-polarized incident waves is based on half-wavelength resonance, that is, the width of the grids is about half of the dielectric wavelength at high band. Thus, it can reflect the EM waves at high band and allow the EM waves at low band to pass. As shown in Fig. 4(a), the transmission magnitude is low than 0.1 at 120 GHz and higher than 0.85 at 75 GHz. The transmission phase with and without grid-B is given in Fig. 4(b). The transmission phase difference between the structure with and without grid-B at 75 GHz is less than 15°. Thus, no additional dielectric layer is added atop of the grid for phase compensating between region II and region IV.

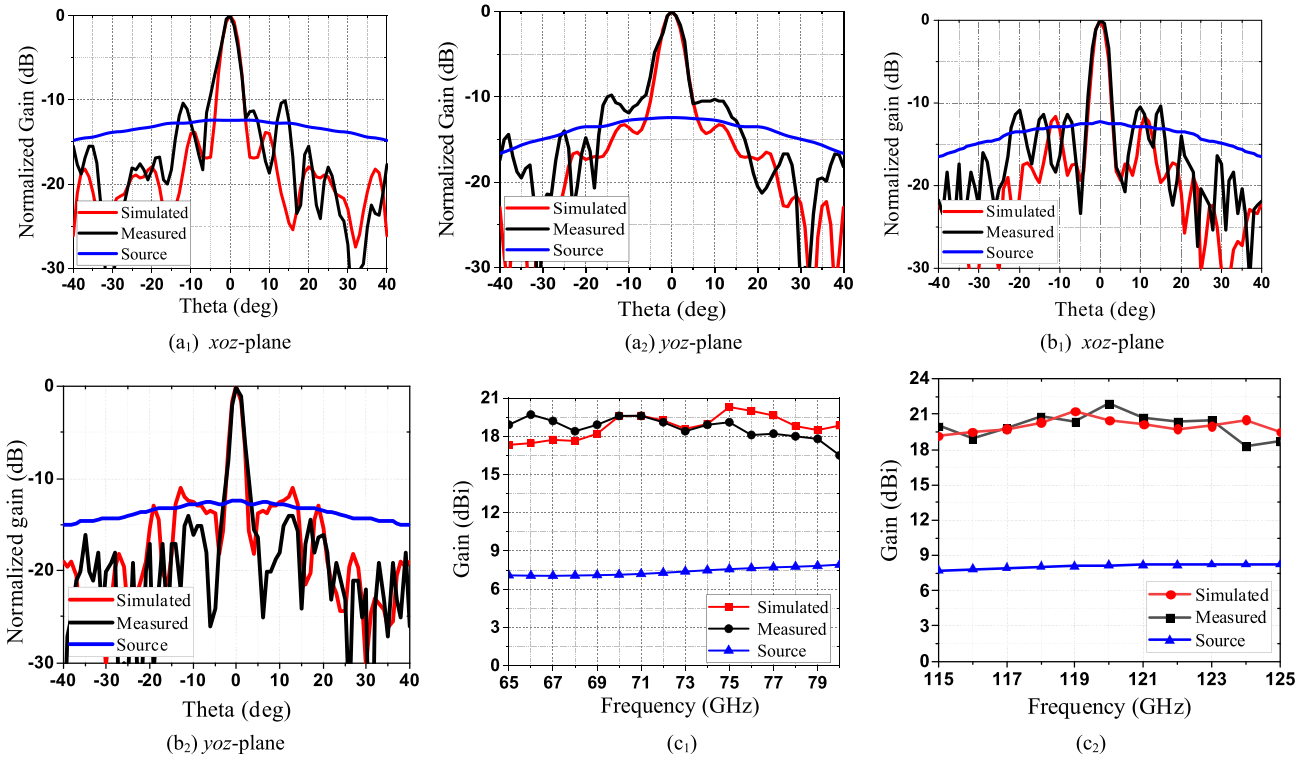

Fig. 10. (a) Simulated and measured radiation patterns at 75 GHz. (b) Simulated and measured radiation patterns at 120 GHz. (c) Simulated and measured boresight gain of the proposed dual-band FZP metalens antenna and the gain of the source at two bands.

C. Dual-Band FZP Lens Antenna

The proposed dual-band metalens is simulated in ANSYS HFSS. Because of the symmetry, only one-quarter of the structure is simulated using symmetry boundary conditions. The convergence criteria of adaptive solution in HFSS simulation are set to be the maximum Delta S < 0.005 at two solution frequencies of 75 and 120 GHz. The number of tetrahedral elements is around 2.2×10^5 and 1.1×10^6 at 75 and 120 GHz, respectively. The focal length is set as 30 mm for both bands with a focal-to-diameter (F/D) ratio of 0.5. The dielectric material is made of ultraviolet (UV) curable acrylates with a dielectric constant of 2.8 and a loss tangent of 0.02 at 120 GHz. The radiation performance of the dual-band FZP metalens antenna at 75 and 120 GHz is compared with that of the single-band FZP metalens antennas A and B, as shown in Figs. 5 and 6. The radiation patterns of the dual-band FZP metalens antenna and single-band FZP metalens antenna A (B) are nearly the same and the boresight gain differences are less than 1 dB, which demonstrates that two FZP metalens antennas are successfully merged into one dual-band FZP metalens antenna with a shared aperture. Figs. 5(b) and 6(b) also give the radiation patterns and gain comparison between the proposed dual-band FZP metalens antenna with and without raised dielectric layers at high band, respectively. It is seen from Fig. 5(b) that after adding the phase compensating rings, the sidelobe levels of the radiation patterns improved from -6 to -12 dB. Meanwhile, the boresight gain improved by 2.4 dB at 120 GHz after adding the phase compensating rings, as shown in Fig. 6(b).

III. Fabrication, Measurement, and Discussion

A. AME Fabrication

The prototype is fabricated using DragonFly 2020 PRO [49], which has two printing heads for metal and dielectric printing, respectively. Each head consists of 512 piezoelectric-based nozzles connecting to an ink-filled chamber (one chamber is filled with silver nanoparticle ink for conductor printing (conductivity of 2×10^7 S/m) and the other is filled with ultraviolet (UV)-curable acrylates ink for dielectric printing. An ultrathin dielectric layer is printed first at the bottom as the soldering mask. Then, the dielectric and conductive inks can be simultaneously jetted to form the dielectric and conductive layer (thickness of 35 μm) according to the pre-designed patterns. Infrared radiation (IR) lamps and UV lights are turned on to solid the silver ink and curable acrylates ink, respectively, as shown in Fig. 7(a) and (b). The prototype of the proposed FZP metalens antenna is shown in Fig. 8, which has a circular aperture with a radius of 32.5 mm.

B. Measurement

The radiation performance is measured using a far-field mm-wave measurement system shown in Fig. 9. The signal from the signal generator is up-converted to 75 and 120 GHz through the frequency extension module. Then, the signal is fed to the dual-band FZP metalens antenna by standard waveguide (WR-12 and WR-07). On the other side, the standard horns are used as the receive antennas at far-field for 75 and 120 GHz, respectively. The receiving horn antenna is

TABLE I
COMPARISON OF STATE-OF-ART FZP LENSES AND OTHER DUAL-BAND LENSES

Ref.	Freq (GHz)	Peak gain	Polarization	Sidelobe level (dB)	Aperture efficiency	Thickness (Normal to the wavelength at low-band)	Fabrication
[23]	Dual-band lens 12.5/14.25 (ratio:1.14)	31/31.8	Dual	-25	45%/41.3%	0.47	PCB
[24]	Dual-band lens 12.5/14.25 (ratio:1.14)	30.2/32.3	Dual	-20	38%/46%	0.48	PCB
[25]	Dual-band lens 19.5/29 (ratio:1.48)	28.1/31	Dual	-20	20.1%/21.2%	0.1	PCB
[26]	Dual-band lens 11/12.5 (ratio:1.14)	23.74/24.45	Dual	-15	38%/34.6%	0.5	PCB
[41]	Single-band focusing FZP lens 32	N.A.	Single	-15	N.A.	0.05	PCB
[44]	Single-band focusing FZP lens 12	N.A.	Single	N.A.	N.A.	0.2	PCB
[45]	Dual-band FZP lens 4.05/5.3 (ratio:1.3)	N.A.	Single	-10	N.A.	0.02	PCB
[46]	Single-band FZP lens 60	32.7	Single	-20	52.8%	9	PCB
[47]	Single-band focusing FZP lens 10	N.A.	Dual	N.A.	N.A.	N.A.	PCB
[52]	Single-band Soret fishnet metalens 96.45	10.64	Single	-15	2%	0.63	PCB
[53]	Single-band Dielectric FZP lens	34.6	Single	-20	52%	1.25	PCB
[54]	Single-band FZP lens 60	27.6	Single	-25	36%	1	Additive manufacturing
[55]	Single-band fishnet metalens 99	20 (simulation) 16.6 (measurement)	Single	-15	3.9% (simulation) 1.8% (measurement)	0.63	PCB
This work	Dual-band FZP lens 75/120 (ratio:1.6)	20.3/21.9	Single	-10	4.8%/2.7%	0.29	Additive manufacturing

connected to a signal analyzer through a frequency extension module. For the gain measurement, two identical standard gain horns are used for making the direct gain comparison to obtain the gain value. The FZP metalens antenna gain (G_{FZP_lens}) can be obtained by [50]

$$\left(G_{FZP\_lens}\right)_{dB} = (G_{horn})_{dB} + 10\log_{10}\left(\frac{P_{FZP\_lens}}{P_{horn}}\right) \quad (2)$$

where G_{horn} is the gain of the standard gain horn, P_{horn} is the received power from the standard gain horn, and P_{FZP_lens} is the received power from the FZP metalens antenna.

The performance of the proposed dual-band FZP metalens antenna is experimentally verified. The simulated and measured radiation patterns at 75 and 120 GHz are given in Fig. 10(a) and (b), respectively, which are matched well. The peak gains are fixed at boresight and the sidelobe levels are kept below -10 dB. The simulated and measured gains at two bands are given in Fig. 10(c). The measured gains are 20.3 dBi at 75 GHz and 21.9 dBi at 120 GHz, respectively. The measurement shows 12.7 and 12.9 dB improvement compared with the waveguide source (WR-12 and WR-07), demonstrating the FZP metalens antenna collimates the beams at two bands.

To analyze the ratio of the portions of regions I, II, III, and IV on the radiation performance, two additional cases with different focal lengths of the FZP metalens are simulated since the portions of regions I, II, III, and IV on the aperture depend on the focal length; see Appendix. For case I, the focal lengths are set as 20 and 30 mm for 75 and 120 GHz bands, respectively. For case II, the focal lengths are set as 30 and 40 mm for 75 and 120 GHz bands, respectively. The results demonstrate that the proposed dual-band FZP metalens solution is still effective when the ratio of the portions of regions I, II, III, and IV changes.

IV. DISCUSSION

Table I compares the proposed dual-band FZP metalens antenna with other related works. The general drawback of metallic FZP lens antenna is the low aperture efficiency because it only uses 0°/180° phase correction, and 50% energy is reflected [47]. Therefore, for the high gain antenna with high aperture efficiency demand, transmitarray antennas with better

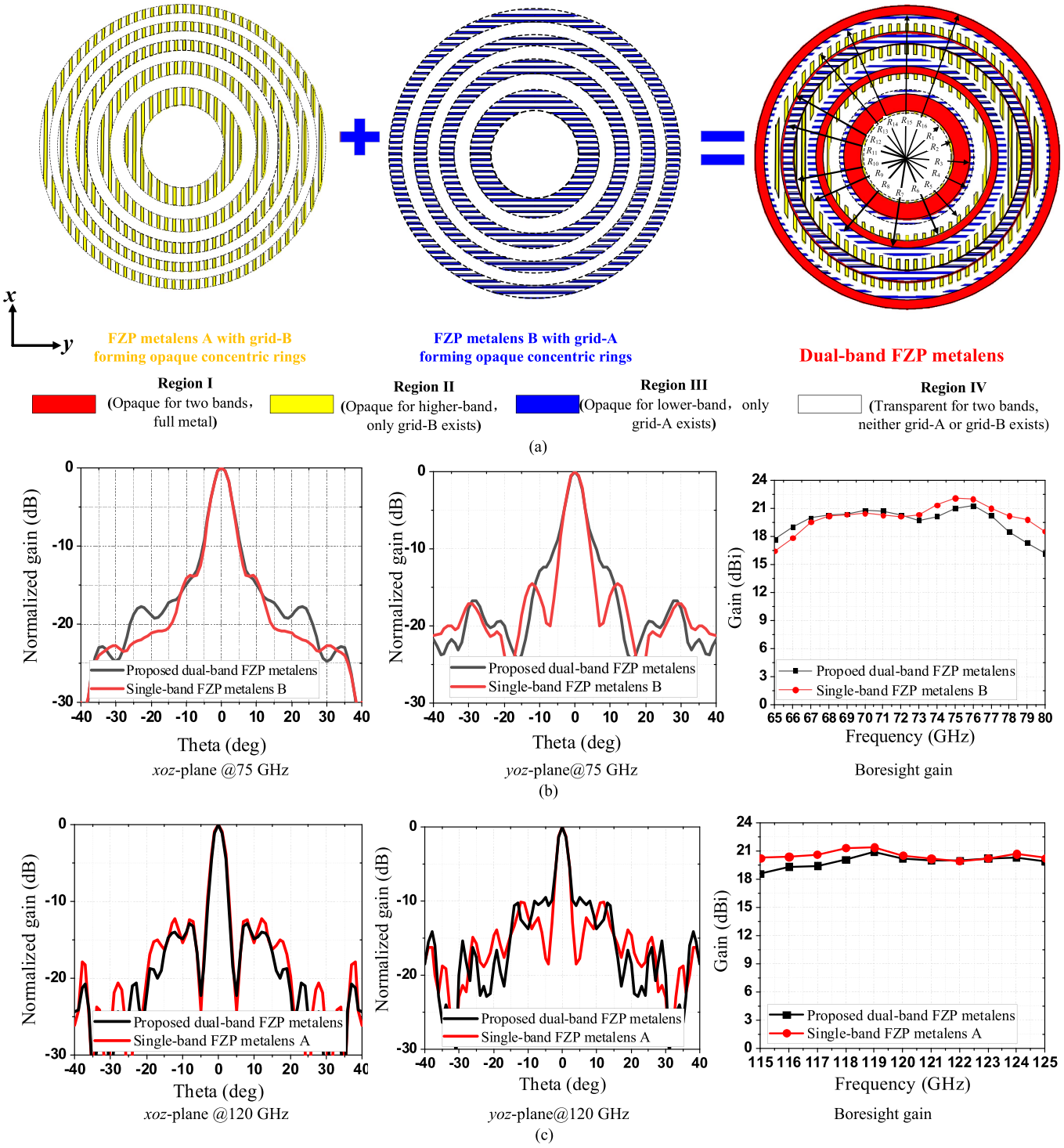

Fig. 11. (a) Configurations of the dual-band FZP metalens antenna. Case I: focal length of 20 mm at 75 GHz band and 30 mm at 120 GHz band (FZP metalens A: operating at the high band and FZP, metalens B: operating at the low band. $R_1 = 8.75$ mm, $R_2 = 9.16$ mm, $R_3 = 12.5$ mm, $R_4 = 13.26$ mm, $R_5 = 15.46$ mm $R_6 = 16.6$ mm, $R_7 = 18$ mm, $R_8 = 19.6$ mm, $R_9 = 20.35$ mm, $R_{10} = 22.5$ mm, $R_{11} = 24.5$ mm, $R_{12} = 24.9$ mm, $R_{13} = 26.5$ mm, $R_{14} = 27.5$ mm, $R_{15} = 28.3$ mm, and $R_{16} = 30$ mm). (b) Radiation patterns and gain comparison between the proposed dual-band FZP metalens antenna and the single-band FZP metalens B at 75 GHz band. (c) Radiation patterns and gain comparison between the proposed dual-band FZP metalens antenna and the single-band FZP metalens A at 120 GHz band.

phase correcting should be used [23]–[26], [51]. Nevertheless, to achieve $[-\pi, \pi]$ full phase correcting, the transmitarrays generally require cascading several resonant phasing elements. This can be easily achieved by stacking several PCB layers in order in the microwave region. However, in the mm-wave/THz band, a complicated bonding structure may be required and the cost increases significantly as the number of layers increases. While the metallic FZP lens antenna basically requires only

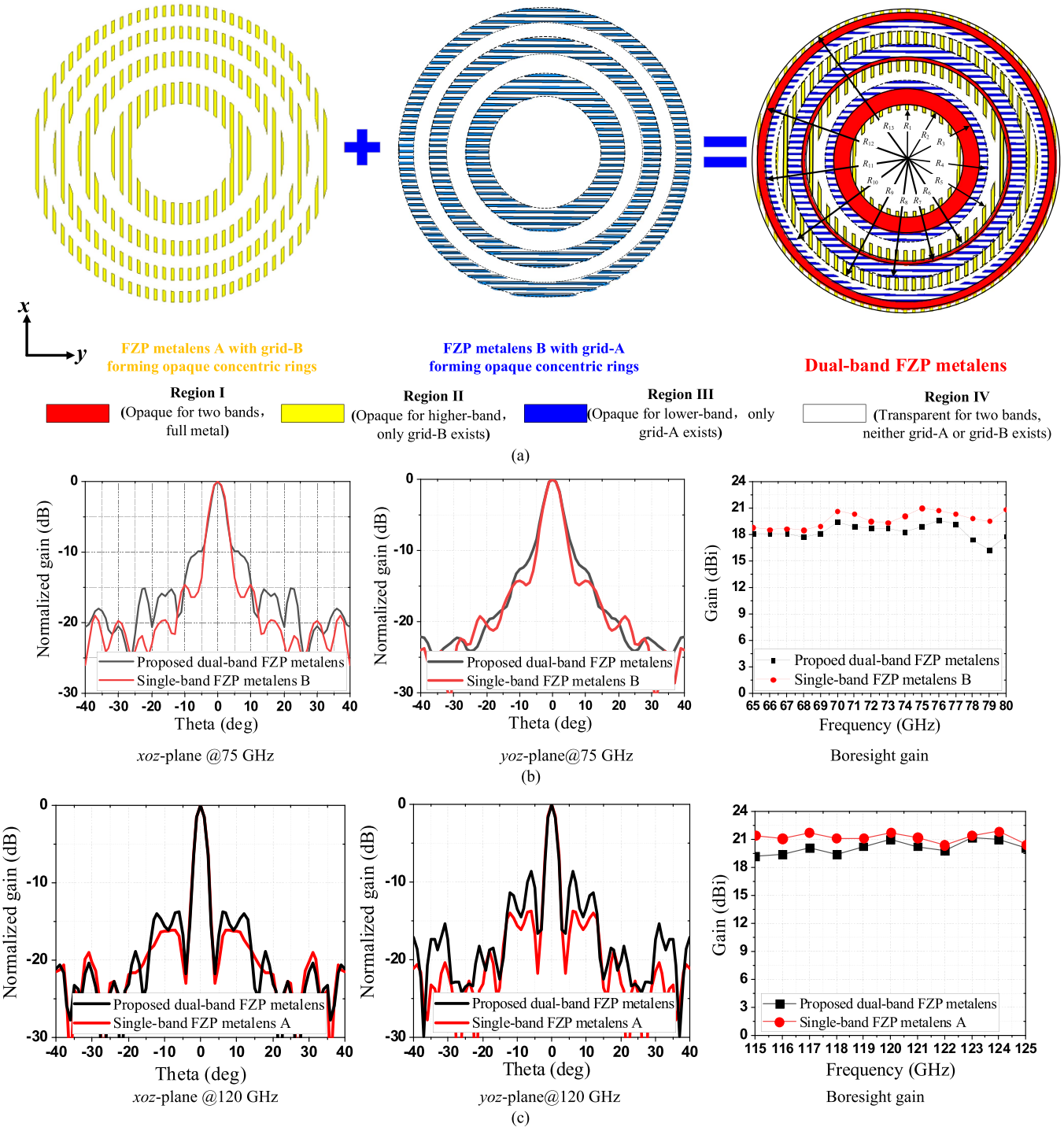

Fig. 12. (a) Configurations of the dual-band FZP metalens antenna. Case II: focal length of 30 mm at 75 GHz band and 40 mm at 120 GHz band (FZP metalens A: operating at the high-band and FZP, metalens B: operating at the low-band. $R_1 = 10.1$ mm, $R_2 = 11.13$ mm, $R_3 = 14.36$ mm, $R_4 = 16$ mm, $R_5 = 17.72$ mm, $R_6 = 19.9$ mm, $R_7 = 20.61$ mm, $R_8 = 23.21$ mm, $R_9 = 25.61$ mm, $R_{10} = 26.46$ mm, $R_{11} = 27.86$ mm, $R_{12} = 29.39$ mm, and $R_{13} = 30$ mm). (b) Radiation patterns and gain comparison between the proposed dual-band FZP metalens antenna and the single-band FZP metalens B at 75 GHz band. (c) Radiation patterns and gain comparison between the proposed dual-band FZP metalens antenna and the single-band FZP metalens A at 120 GHz band.

one or two metal layers. Therefore, in some scenarios where antenna layers are restricted, and aperture efficiency is not the primary concern, the FZP lens antenna can be a good substitute for the transmitarray antenna.

Because of the frequency-dependent feature, previous FZP lens antennas are limited to a single band [41], [44], [46]. Although a reconfigurable dual-band FZP lens is proposed using switch [45], only high gain at one band can generate

on the aperture at a given state. In addition, the lossy pin diodes hinder the concept from being applied to the mm-wave regions. Because it is difficult for the phasing element to achieve dual-band/multiband phase control of the wavefront independently in a single polarization, most of the lenses use polarization to provide a more degree of freedom to realize dual band [23], [26], [47]. In contrast, the proposed ultra-thin FZP metalens antenna can operate at two bands with the same polarization. The radiation performance at the two bands is comparable to that of each single FZP metalens antenna. Regarding the frequency ratio, the current unit cells forming the opaque region are suitable for a relatively large frequency ratio. To achieve a very small frequency ratio, unit cells with higher frequency selectivity can be used, but the number of the layers may increase as well.

The general advantage of the dielectric/metal joint printing over PCB fabrication is that: 1) multiple metal layers can be printed in a single dielectric substrate with fewer constraints of the distance between metal layers; 2) no bonding process is required among multiple metal layers; and 3) the fabrication cost will not increase as the layer increases. The 3-D printing solution provides the designers with more design flexibility than the traditional multilayer PCB solutions, especially for designs with small form factor expectations at mm-wave and THz frequencies. Take the proposed design as an example, to compensate for the metagrids' phase shift, an additional dielectric ring layer is added atop the FZP. The dielectric ring layer can be easily and seamlessly printed on the top of the metallic layer. In contrast, a bonding structure is required if the PCB solution is used. Besides, the distance between the metallic layers and the dielectric layer thickness can be flexibly selected to meet the desired dimensions, which cannot be easily achieved using PCB or low-temperature co-fire ceramics (LTCC) solutions.

V. Conclusion

In summary, a shared aperture dual-band FZP metalens antenna operating at 75 and 120 GHz is proposed and experimentally verified. The concentric rings of two FZP metalens antennas made of different kinds of grid polarizers are merged seamlessly, forming the dual-band FZP metalens antenna in a shared aperture. High directional radiation is achieved at two bands with the measured peak gains of 20.3 and 21.9 dBi at 75 and 120 GHz, respectively. The proposed FZP metalens antenna has the merits of lightweight, low profile, and fast-prototyped using conductive/dielectric integrated AME technique. Potential applications of the FZP metalens antenna include multiband mm-wave communications, sensing, and imaging.

Appendix

Two FZP metalenses with different focal lengths are simulated for further demonstration. For case I, the focal lengths are set as 20 and 30 mm for 75 and 120 GHz band, respectively. The configuration of the metalens is given in Fig. 11(a), and the radiation patterns and gain comparison are given in Fig. 11(b) and (c). For case II, the focal lengths are set as 30 and 40 mm for 75 and 120 GHz band, respectively. The configuration of the metalens is given in Fig. 12(a), and the radiation patterns and gain comparison are given in Fig. 12(b) and (c).

References

[1] M. Tonouchi, "Cutting-edge terahertz technology," *Nature Photon.*, vol. 1, no. 2, pp. 97–105, Feb. 2007.

[2] S. van Berkel, O. Yurduseven, A. Freni, A. Neto, and N. Llombart, "THz imaging using uncooled wideband direct detection focal plane arrays," *IEEE Trans. THz Sci. Technol.*, vol. 7, no. 5, pp. 481–492, Sep. 2017.

[3] K. B. Cooper *et al.*, "Penetrating 3-D imaging at 4- and 25-m range using a submillimeter-wave radar," *IEEE Trans. Microw. Theory Technol.*, vol. 56, no. 12, pp. 2771–2778, Dec. 2008.

[4] R. T. Ako, A. Upadhyay, W. Withayachumnankul, M. Bhaskaran, and S. Sriram, "Dielectrics for terahertz metasurfaces: Material selection and fabrication techniques," *Adv. Opt. Mater.*, vol. 8, no. 3, Feb. 2020, Art. no. 1900750.

[5] H.-J. Song and T. Nagatsuma, "Present and future of terahertz communications," *IEEE Trans. THz Sci. Technol.*, vol. 1, no. 1, pp. 256–263, Sep. 2011.

[6] B. Zhang, Y.-X. Guo, H. Zirath, and Y. P. Zhang, "Investigation on 3-D-printing technologies for millimeter-wave and terahertz applications," *Proc. IEEE*, vol. 105, no. 4, pp. 723–736, Apr. 2017.

[7] K. Delfanazari, R. A. Klemm, H. J. Joyce, D. A. Ritchie, and K. Kadowaki, "Integrated, portable, tunable, and coherent terahertz sources and sensitive detectors based on layered superconductors," *Proc. IEEE*, vol. 108, no. 5, pp. 721–734, May 2020.

[8] D. Headland, Y. Monnai, D. Abbott, C. Fumeaux, and W. Withayachumnankul, "Tutorial: Terahertz beamforming, from concepts to realizations," *APL Photon.*, vol. 3, no. 5, May 2018, Art. no. 051101.

[9] W. J. Otter and S. Lucyszyn, "Hybrid 3-D-printing technology for tunable THz applications," *Proc. IEEE*, vol. 105, no. 4, pp. 756–767, Apr. 2017.

[10] T. Kleine-Ostmann and T. Nagatsuma, "A review on terahertz communications research," *J. Infr., Millim., THz Waves*, vol. 32, no. 2, pp. 143–171, Feb. 2011.

[11] P. Mei, S. Zhang, X. Q. Lin, and G. F. Pedersen, "A millimeter-wave gain-filtering transmitarray antenna design using a hybrid lens," *IEEE Antennas Wireless Propag. Lett.*, vol. 18, no. 7, pp. 1362–1366, Jul. 2019.

[12] M. Chen, A. Epstein, and G. V. Eleftheriades, "Design and experimental verification of a passive Huygens' metasurface lens for gain enhancement of frequency-scanning slotted-waveguide antennas," *IEEE Trans. Antennas Propag.*, vol. 67, no. 7, pp. 4678–4692, Jul. 2019.

[13] P. Nayeri, F. Yang, and A. Z. Elsherbeni, *Reflectarray Antennas: Theory, Designs, and Applications*. Hoboken, NJ, USA: Wiley, 2018.

[14] S.-W. Qu, H. Yi, B. J. Chen, K. B. Ng, and C. H. Chan, "Terahertz reflecting and transmitting metasurfaces," *Proc. IEEE*, vol. 105, no. 6, pp. 1166–1184, Jun. 2017.

[15] S. Liu *et al.*, "Free-standing metasurfaces for high-efficiency transmitarrays for controlling terahertz waves," *Adv. Opt. Mater.*, vol. 4, no. 3, pp. 384–390, Mar. 2016.

[16] C. Jouanlanne *et al.*, "Wideband linearly polarized transmitarray antenna for 60 GHz backhauling," *IEEE Trans. Antennas Propag.*, vol. 65, no. 3, pp. 1440–1445, Mar. 2017.

[17] C. Xue, Q. Lou, and Z. N. Chen, "Broadband double-layered Huygens' metasurface lens antenna for 5G millimeter-wave systems," *IEEE Trans. Antennas Propag.*, vol. 68, no. 3, pp. 1468–1476, Mar. 2020.

[18] Z. H. Jiang, Y. Zhang, J. Xu, Y. Yu, and W. Hong, "Integrated broadband circularly polarized multibeam antennas using berry-phase transmitarrays for Ka-band applications," *IEEE Trans. Antennas Propag.*, vol. 68, no. 2, pp. 859–872, Feb. 2020.

[19] S. L. Liu, X. Q. Lin, Z. Q. Yang, Y. J. Chen, and J. W. Yu, "W-band low-profile transmitarray antenna using different types of fss units," *IEEE Trans. Antennas Propag.*, vol. 66, no. 9, pp. 4613–4619, Sep. 2018.

[20] M. Jiang, Z. N. Chen, Y. Zhang, W. Hong, and X. Xuan, "Metamaterial-based thin planar lens antenna for spatial beamforming and multibeam massive MIMO," *IEEE Trans. Antennas Propag.*, vol. 65, no. 2, pp. 464–472, Feb. 2017.

[21] J. Wang *et al.*, "Metantenna: When metasurface meets antenna again," *IEEE Trans. Antennas Propag.*, vol. 68, no. 3, pp. 1332–1347, Mar. 2020.

[22] Z. Shi, S. Yang, S. Qu, and Y. Chen, "Circularly polarised planar Luneberg lens antenna for mm-wave wireless communication," *Electron. Lett.*, vol. 52, no. 15, pp. 1281–1282, Jul. 2016.
[23] A. Aziz, F. Yang, S. Xu, and M. Li, "An efficient dual-band orthogonally polarized transmitarray design using three-dipole elements," *IEEE Antennas Wireless Propag. Lett.*, vol. 17, no. 2, pp. 319–322, Feb. 2018.
[24] A. Aziz, F. Yang, S. Xu, M. Li, and H.-T. Chen, "A high-gain dual-band and dual-polarized transmitarray using novel loop elements," *IEEE Antennas Wireless Propag. Lett.*, vol. 18, no. 6, pp. 1213–1217, Jun. 2019.
[25] K. T. Pham, R. Sauleau, E. Fourn, F. Diaby, A. Clemente, and L. Dussopt, "Dual-band transmitarrays with dual-linear polarization at Ka-band," *IEEE Trans. Antennas Propag.*, vol. 65, no. 12, pp. 7009–7018, Dec. 2017.
[26] M. O. Bagheri, H. R. Hassani, and B. Rahmati, "Dual-band, dual-polarised metallic slot transmitarray antenna," *IET Microw., Antennas Propag.*, vol. 11, no. 3, pp. 402–409, Feb. 2017.
[27] C. Wang, J. Wu, and Y.-X. Guo, "A 3-D-printed multibeam dual circularly polarized luneburg lens antenna based on quasi-icosahedron models for Ka-band wireless applications," *IEEE Trans. Antennas Propag.*, vol. 68, no. 8, pp. 5807–5815, Aug. 2020.
[28] M. F. Farooqui and A. Shamim, "3-D inkjet-printed helical antenna with integrated lens," *IEEE Antennas Wireless Propag. Lett.*, vol. 16, pp. 800–803, 2017.
[29] H. Yi, S.-W. Qu, K.-B. Ng, C. H. Chan, and X. Bai, "3-D printed millimeter-wave and terahertz lenses with fixed and frequency scanned beam," *IEEE Trans. Antennas Propag.*, vol. 64, no. 2, pp. 442–449, Feb. 2016.
[30] A. C. Paolella, C. D. Fisher, C. Corey, D. Foster, and D. Silva-Saez, "3-D printed millimeter-wave lens systems at 39 GHz," *IEEE Microw. Wireless Compon. Lett.*, vol. 28, no. 6, pp. 464–466, Jun. 2018.
[31] G.-B. Wu, Y.-S. Zeng, K. F. Chan, S.-W. Qu, and C. H. Chan, "3-D printed circularly polarized modified fresnel lens operating at terahertz frequencies," *IEEE Trans. Antennas Propag.*, vol. 67, no. 7, pp. 4429–4437, Jul. 2019.
[32] B. Zhang *et al.*, "A K-band 3D printed focal-shifted two-dimensional beam scanning lens antenna with non-uniform feed," *IEEE Antennas Wireless Propag. Lett.*, vol. 18, no. 12, pp. 2721–2725, Dec. 2019.
[33] Y. Li, L. Ge, M. Chen, Z. Zhang, Z. Li, and J. Wang, "Multibeam 3-D-Printed luneburg lens fed by magnetoelectric dipole antennas for millimeter-wave MIMO applications," *IEEE Trans. Antennas Propag.*, vol. 67, no. 5, pp. 2923–2933, May 2019.
[34] J. M. Monkevich and G. P. Le Sage, "Design and fabrication of a custom-dielectric fresnel multi-zone plate lens antenna using additive manufacturing techniques," *IEEE Access*, vol. 7, pp. 61452–61460, 2019.
[35] J. Budhu and Y. Rahmat-Samii, "3D-printed inhomogeneous dielectric lens antenna diagnostics: A tool for assessing lenses misprinted due to fabrication tolerances," *IEEE Antennas Propag. Mag.*, vol. 62, no. 4, pp. 49–61, Aug. 2020.
[36] J. Zhu *et al.*, "3-D printed planar dielectric linear-to-circular polarization conversion and beam-shaping lenses using coding polarizer," *IEEE Trans. Antennas Propag.*, vol. 68, no. 6, pp. 4332–4343, Jun. 2020.
[37] M. K. T. Al-Nuaimi and W. Hong, "Discrete dielectric reflectarray and lens for E-band with different feed," *IEEE Antennas Wireless Propag. Lett.*, vol. 13, pp. 947–950, 2014.
[38] K. X. Wang and H. Wong, "Design of a wideband circularly polarized millimeter-wave antenna with an extended hemispherical lens," *IEEE Trans. Antennas Propag.*, vol. 66, no. 8, pp. 4303–4308, Aug. 2018.
[39] H. Xin and M. Liang, "3-D-Printed microwave and THz devices using polymer jetting techniques," *Proc. IEEE*, vol. 105, no. 4, pp. 737–755, Apr. 2017.
[40] H. Qiao *et al.*, "Compact terahertz detector based on lightweight 3D-printed lens packaging," *Electron. Lett.*, vol. 55, no. 14, pp. 796–797, Jul. 2019.
[41] S. Karimkashi and A. A. Kishk, "Focusing properties of fresnel zone plate lens antennas in the near-field region," *IEEE Trans. Antennas Propag.*, vol. 59, no. 5, pp. 1481–1487, May 2011.
[42] H. D. Hristov, L. P. Kamburov, J. R. Urumov, and R. Feick, "Focusing characteristics of curvilinear half-open fresnel zone plate lenses: Plane wave illumination," *IEEE Trans. Antennas Propag.*, vol. 53, no. 6, pp. 1912–1919, Jun. 2005.
[43] H. D. Hristov, *Fresnel Zones in Wireless Links, Zone Plate Lenses, and Antennas*. Boston, MA, USA: Artech House, 2000.
[44] Y. Fan, B.-L. Ooi, H. D. Hristov, and M.-S. Leong, "Compound diffractive lens consisting of fresnel zone plate and frequency selective screen," *IEEE Trans. Antennas Propag.*, vol. 58, no. 6, pp. 1842–1847, Jun. 2010.
[45] H. Li *et al.*, "Dual-band fresnel zone plate antenna with independently steerable beams," *IEEE Trans. Antennas Propag.*, vol. 66, no. 4, pp. 2113–2118, Apr. 2018.
[46] M. R. D. Kodnoeih, Y. Letestu, R. Sauleau, E. M. Cruz, and A. Doll, "Compact folded fresnel zone plate lens antenna for mm-wave communications," *IEEE Antennas Wireless Propag. Lett.*, vol. 17, no. 5, pp. 873–876, May 2018.
[47] H. Markovich, D. Filonov, I. Shishkin, and P. Ginzburg, "Bifocal fresnel lens based on the polarization-sensitive metasurface," *IEEE Trans. Antennas Propag.*, vol. 66, no. 5, pp. 2650–2654, May 2018.
[48] A. F. Kurtz, R. Sujatha, and M. I. Xiang-Dong, "Wire grid polarizer," U.S. Patent 6 665 119, Dec. 16, 2003.
[49] *DragonFly LDM Lights-Out Digital Manufacturing System*. Accessed: Apr. 10, 2021. [Online]. Available: https://www.nano-di.com/ame-dragonfly-ldm
[50] C. A. Balanis, *Antenna Theory Analysis and Design*. New York, NY, USA: Wiley, 1997.
[51] S. A. Matos *et al.*, "High gain dual-band beam-steering transmit array for satcom terminals at Ka-band," *IEEE Trans. Antennas Propag.*, vol. 65, no. 7, pp. 3528–3539, Jul. 2017.
[52] B. Orazbayev, M. Beruete, V. Pacheco-Peña, G. Crespo, J. Teniente, and M. Navarro-Cía, "Soret fishnet metalens antenna," *Sci. Rep.*, vol. 5, no. 1, May 2015, Art. no. 9988.
[53] A. Jouade, J. Bor, M. Himdi, and O. Lafond, "Millimeter-wave fresnel zone plate lens with new technological process," *Int. J. Microw. Wireless Technol.*, vol. 9, no. 4, pp. 939–944, May 2017.
[54] J. Pourahmadazar and T. A. Denidni, "Towards millimeter-wavelength: Transmission-mode fresnel-zone plate lens antennas using plastic material porosity control in homogeneous medium," *Sci. Rep.*, vol. 8, no. 1, Mar. 2018, Art. no. 5300.
[55] B. Orazbayev, M. Beruete, and M. Navarro-Cía, "Wood zone plate fishnet metalens," *EPJ Appl. Metamaterials*, vol. 2, p. 8, Dec. 2015.

Jianfeng Zhu (Member, IEEE) was born in Changsha, China. He received the B.Eng. degree in communication engineering from the Beijing University of Posts and Telecommunications (BUPT), Beijing, China, in 2013. He is currently pursuing the joint Ph.D. degree with BUPT and the University of Technology Sydney (UTS), Ultimo, NSW, Australia.

From November 2015 to June 2018, he was a Research Assistant with the State Key Laboratory of Millimeter Waves, Department of Electronic Engineering, City University of Hong Kong, Hong Kong. Since 2018, he has been a Visiting Scholar with the South China University of Technology (SCUT), Guangzhou, China, with the research of LTCC and antenna-in-package. He has authored and coauthored more than 40 journal and conference articles. His current research includes THz/sub-THz beam shaping and 3-D printing.

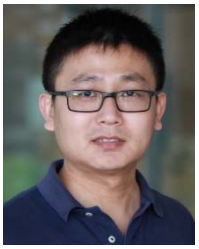

Yang Yang (Senior Member, IEEE) received the M.Eng., M.Sc., and Ph.D. degrees from the Department of Electrical and Computer Systems Engineering (ECSE), Clayton Campus, Monash University, Clayton, VIC, Australia, in 2007, 2008, and 2013, respectively.

He has three years of industrial experience with Rain Bird Australia serving as an Asia–Pacific GSP Engineer, from 2012 to 2015. He received the corporate 2014 Global GSP Success Award (one globally). In April 2015, he returned to academia and served as a Senior Research Associate with the Centre for Collaboration in Electromagnetic and Antenna Engineering, Macquarie University. In April 2016, he was appointed as a Research Fellow with the State Key Laboratory of Terahertz and Millimeter Waves, City University of Hong Kong, Hong Kong. Since December 2016, he joined the University of Technology Sydney. He is currently a Senior Lecturer and a Team Leader of millimeter-wave integrated circuits and antennas. He has over 150 international peer-reviewed publications in microwave and millimeter-wave circuits and antennas. His research interests include millimeter-wave and sub-terahertz technologies in 5G and biomedical applications.

Dr. Yang is a Committee Member of MTT-28 Biological Effects and Medical Applications. He is a winner of CST University Publication Award 2018, by CST, Dassault Systèmes. He is an Associate Editor of IEEE ACCESS and an Area Editor (Track Editor) of *Microwave and Optical Technology Letters*.

Mengze Li (Student Member, IEEE) was born in Hunan, China, in 1994. She received the B.Eng. degree in electrical engineering and automation from Hunan University, Hunan, China, in 2015, and the M.Eng. degree in electronic field and microwave technology from Xiamen University, Xiamen, China, in 2018. She is currently pursuing the Ph.D. degree with the University of Technology Sydney.

From 2017 to 2018, she was a Visiting Student with the Faculty of Engineering and Information Technology, University of Technology Sydney, Ultimo NSW, Australia, where she is currently pursuing the Ph.D. degree. Her current research interests include microstrip filters, multiplexers, RFIC, and 3-D print technology.

David McGloin received the M.Sci. degree (Hons.) in laser physics and optoelectronics and the Ph.D. degree in laser and atomic physics from the University of St. Andrews, St Andrews, U.K., in 1997 and 2001, respectively.

He was a Post-Doctoral Research Fellowship in atom optics with St. Andrews, in 2002. He was with the UK Defense Science and Technology Laboratory, Fort Halstead. He was awarded a Royal Society University Research Fellowship from 2003 to 2011. He was a Visiting Scholar with the University of Washington in Seattle, in 2006. He took up a Lectureship in the Division of Physics, University of Dundee, U.K., in 2007, and subsequently he was a Senior Lecturer and a Reader. He was also the Head of physics and the Associate Dean for Research with the School of Science and Engineering, Dundee. He joined UTS in Sydney in 2018 as a Professor of Optical Physics and Director of Research Programs in the Faculty of Engineering and IT. His current research interests include optical trapping and manipulation, optical and THz beam shaping, aerosol science, biophotonics, microscopy, and Raman spectroscopy. He has authored more than 80 peer-reviewed articles.

Dr. McGloin is a Senior Member of the Optical Society of America and a member of the Institute of Physics.

Shaowei Liao (Senior Member, IEEE) received the Ph.D. degree in electromagnetic fields and microwave technology from the University of Electronic Science and Technology of China (UESTC), Chengdu, China, in 2010.

In 2011, he joined the School of Electronic Engineering, UESTC, as a Lecturer. From 2011 to 2012, he was a Senior Research Associate with the Department of Electronic Engineering, City University of Hong Kong, Hong Kong. From 2012 to 2013, he was a Research Scientist with Bell Labs Research, Shanghai Bell, Alcatel-Lucent, China. From 2013 to 2017, he was an Engineer with the State Key Laboratory of Millimeter Waves, City University of Hong Kong. He is currently an Associate Professor with the School of Electronics and Information Engineering, South China University of Technology. He has authored or coauthored more than 30 articles on IEEE journals. He is a co-inventor of five granted U.S. and European patents. His current research interests include various antennas, microwave components, and computational electromagnetics.

Dr. Liao is a Reviewer for the IEEE TRANSACTIONS ON ANTENNAS AND PROPAGATION, the IEEE ANTENNAS AND WIRELESS PROPAGATION LETTERS, and the IEEE MICROWAVE AND WIRELESS COMPONENTS LETTERS. He is the winner of 2017 H.A. Wheeler Applications Prize Paper Award.

Jaim Nulman (Senior Member, IEEE) received the bachelor's degree in electrical engineering from the Technion-Israel Institute of Technology, Haifa, Israel, in 1979, the master's and Ph.D. degrees in electrical engineering from Cornell University, Ithaca, NY, USA, in 1982 and 1984, respectively, and the MBA degree from Stanford University, Stanford, CA, USA, in 1994.

He is a Proven Influencer and Innovator with more than 30 years of expertise in working with companies from start-ups to Fortune 500 enterprises. He served as a Vice President of Applied Materials, where he spent 15 years in several product division and corporate positions. He drove the successful commercialization of one of Applied Materials' semiconductor manufacturing products with impressive market penetration of $1 billion in less than five years. He is a Co-Inventor in over 30 patents in the area of semiconductor manufacturing technology, semiconductor manufacturing equipment, and additive manufacturing for electronics. He has served as Invited Lecturer with UC Berkeley extension and NATO's International Summer Institute.

Minoru Yamada was born in Toyama, Japan, in 1952. He was involved in Electronics Product Development for more than 40 years, especially wireless telecommunication products such as voice and video data transfer system using DECT Technology. He developed more than 50 products and sold in market under British telecom, Motorola, Philips, Uniden, Telstra, and some other brands. His responsibility was mainly RF hardware and software development. For the past 20 years, he was mainly managing the research and development department and product architecture development.

Francesca Iacopi (Senior Member, IEEE) has over 20 years of international industrial and academic expertise in the miniaturization of semiconductor technologies. She has led large research and development projects for IMEC, Belgium, and Globalfoundries Inc., USA, in interconnects, electronic devices, and packaging. Her focus is the translation of basic scientific advances into nanomaterials and device concepts into integrated technologies. She is known for her work in porous dielectrics for interconnects, and, more recently, graphene for ON-chip applications. She leads the Integrated Nanosystems Lab, in the Faculty of Engineering and IT, University of Technology Sydney, and is a Chief Investigator of the ARC Center of Excellence in Transformative Meta-Optical Systems (TMOS).

Ms. Iacopi is a fellow of the Institution of Engineers Australia and currently serves in several technical committees for the Materials Research Society, the IEEE Electron Devices Society, and the International Roadmap for Systems and Devices. She is a recipient of the MRS Gold Graduate Student Award in 2003, the ARC Future Fellowship in 2012, and the Global Innovation Award in Washington DC in 2014, and she was listed among the most innovative engineers by Engineers Australia in 2018.